REPORT DOCUMENTATION PAGE

Form Approved OMB NO. 0704-0188

1. REPORT DATE (DD-MM-YYYY)	2. REPORT TYPE	3. DATES COVERED (From - To)
	New Reprint	-

4. TITLE AND SUBTITLE
Nitrogen: unraveling the secret to stable carbon-supported Pt-alloy electrocatalysts

5a. CONTRACT NUMBER
W911NF-09-1-0528

5b. GRANT NUMBER

5c. PROGRAM ELEMENT NUMBER
611103

6. AUTHORS
Svitlana Pylypenko, Albina Borisevich, Karren L. More, April R. Corpuz, Timothy Holme, Tim S. Olson, Huyen N. Dinh, Thomas Gennett, Ryan O'Hayre, Arrelaine A. Dameron

5d. PROJECT NUMBER

5e. TASK NUMBER

5f. WORK UNIT NUMBER

7. PERFORMING ORGANIZATION NAMES AND ADDRESSES
Colorado School of Mines
1500 Illinois St

Golden, CO 80401 -1911

8. PERFORMING ORGANIZATION REPORT NUMBER

9. SPONSORING/MONITORING AGENCY NAME(S) AND ADDRESS (ES)
U.S. Army Research Office
P.O. Box 12211
Research Triangle Park, NC 27709-2211

10. SPONSOR/MONITOR'S ACRONYM(S)
ARO

11. SPONSOR/MONITOR'S REPORT NUMBER(S)
54646-CH-PCS.28

12. DISTRIBUTION AVAILIBILITY STATEMENT
Approved for public release; distribution is unlimited.

13. SUPPLEMENTARY NOTES
The views, opinions and/or findings contained in this report are those of the author(s) and should not contrued as an official Department of the Army position, policy or decision, unless so designated by other documentation.

14. ABSTRACT
Nitrogen functionalities significantly improve performance for metal-based carbon-supported catalysts, yet their specific role is not well understood. In this work, a direct observation of the nanoscale spatial relationship between surface nitrogen and metal catalyst nanoparticles on a carbon support is established through principal component analysis (PCA) of electron energy loss spectral (EELS) imaging datasets acquired on an aberration-corrected scanning transmission electron microscope (STEM). Improved catalyst–support interactions correlated to high substrate nitrogen content in immediate proximity to stabilized nanoparticles are first demonstrated using model

15. SUBJECT TERMS
nitrogen, carbon, electrocatalysis, microscopy, eels, direct methanol fuel cells

16. SECURITY CLASSIFICATION OF:			17. LIMITATION OF ABSTRACT	15. NUMBER OF PAGES	19a. NAME OF RESPONSIBLE PERSON
a. REPORT	b. ABSTRACT	c. THIS PAGE			Ryan O'Hayre
UU	UU	UU	UU		19b. TELEPHONE NUMBER: 303-273-3952

Report Title

Nitrogen: unraveling the secret to stable carbon-supported Pt-alloy electrocatalysts

ABSTRACT

Nitrogen functionalities significantly improve performance for metal-based carbon-supported catalysts, yet their specific role is not well understood. In this work, a direct observation of the nanoscale spatial relationship between surface nitrogen and metal catalyst nanoparticles on a carbon support is established through principal component analysis (PCA) of electron energy loss spectral (EELS) imaging datasets acquired on an aberration-corrected scanning transmission electron microscope (STEM). Improved catalyst–support interactions correlated to high substrate nitrogen content in immediate proximity to stabilized nanoparticles are first demonstrated using model substrates. These insights are applied in direct methanol fuel cell prototypes to achieve substantial improvements in performance and long-term stability using both in-house and commercial catalysts doped with nitrogen. These results have immediate impact in advanced design and optimization of next generation high performance catalyst materials.

REPORT DOCUMENTATION PAGE (SF298)
(Continuation Sheet)

Continuation for Block 13

ARO Report Number 54646.28-CH-PCS
Nitrogen: unraveling the secret to stable carbon-...

Block 13: Supplementary Note

Approved for public release; distribution is unlimited.

Energy & Environmental Science

www.rsc.org/ees

Volume 6 | Number 10 | October 2013 | Pages 2779–3100

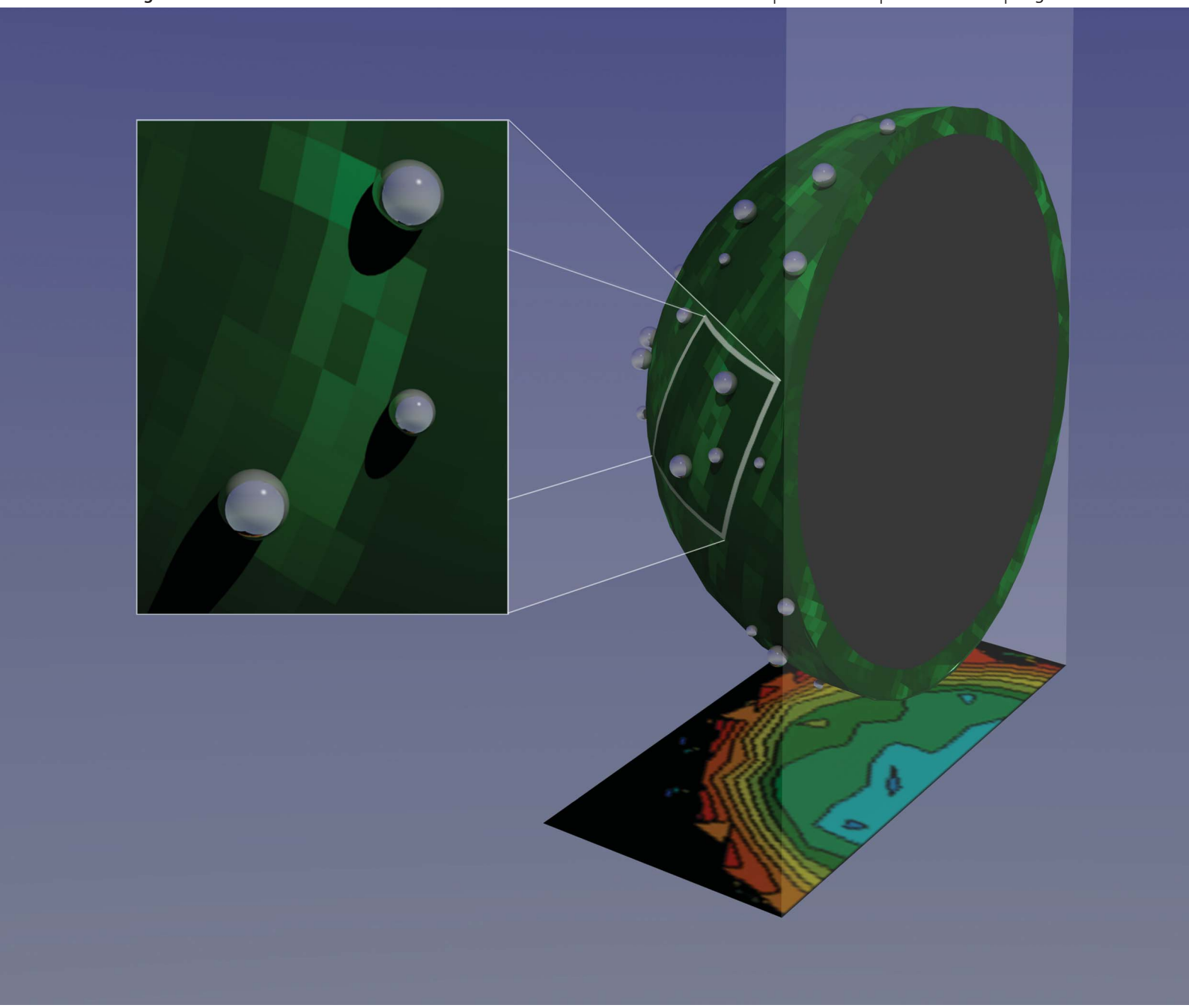

ISSN 1754-5692

RSC Publishing

PAPER

O'Hayre *et al.*

Nitrogen: unravelling the secret to stable carbon-supported Pt-alloy electrocatalysts

1754-5692(2013)6:10;1-0

Energy & Environmental Science

RSC Publishing

PAPER

View Article Online
View Journal | View Issue

Nitrogen: unraveling the secret to stable carbon-supported Pt-alloy electrocatalysts

Cite this: *Energy Environ. Sci.*, 2013, **6**, 2957

Svitlana Pylypenko,[a] Albina Borisevich,[b] Karren L. More,[b] April R. Corpuz,[c] Timothy Holme,[d] Arrelaine A. Dameron,[e] Tim S. Olson,[e] Huyen N. Dinh,[e] Thomas Gennett[e] and Ryan O'Hayre*[a]

Received 19th January 2013
Accepted 1st March 2013

DOI: 10.1039/c3ee40189h

www.rsc.org/ees

Nitrogen functionalities significantly improve performance for metal-based carbon-supported catalysts, yet their specific role is not well understood. In this work, a direct observation of the nanoscale spatial relationship between surface nitrogen and metal catalyst nanoparticles on a carbon support is established through principal component analysis (PCA) of electron energy loss spectral (EELS) imaging datasets acquired on an aberration-corrected scanning transmission electron microscope (STEM). Improved catalyst–support interactions correlated to high substrate nitrogen content in immediate proximity to stabilized nanoparticles are first demonstrated using model substrates. These insights are applied in direct methanol fuel cell prototypes to achieve substantial improvements in performance and long-term stability using both *in-house* and commercial catalysts doped with nitrogen. These results have immediate impact in advanced design and optimization of next generation high performance catalyst materials.

Introduction

Heterogeneous catalysis often requires costly nanostructured materials and while their performance characteristics[1–8] continue to improve; they are susceptible to morphological changes that reduce catalytic performance during operation. In the case of polymer–electrolyte fuel cells, state-of-the-art electrocatalysts made from high surface area carbon materials decorated with a precious-metal nanoparticle phase often exhibit rapid initial-stage activity loss caused by irreversible changes in catalyst surface area, structure, and composition.[9] Various solutions of decreasing cost while increasing electrocatalytic activity and durability have been proposed, including modification of the precious-metal-based phase to decrease the amount of precious metal through core–shell structures,[1,10,11] improve catalyst utilization with extended surfaces[2] and/or the replacement of the noble metal-based catalyst with non-noble alternatives.[3,4,12]

Another route to enhanced performance is to improve the catalyst–substrate interaction through functionalization of the carbon matrix with heteroatoms such as nitrogen and boron.[13,14] Several classes of nitrogen-containing carbon-matrix materials utilized in polymer electrolyte fuel cells (PEFCs) and direct methanol fuel cells (DMFCs), including Pt-based cathodes, PtRu anodes, and various non-precious materials, have been shown to outperform analogous non-nitrogen containing catalyst materials.[3,4,12–24] For nearly a decade it has been hypothesized that carbon supports doped with nitrogen improve catalyst–support interactions by improving dispersion, durability, and catalytic activity of the overlying Pt-nanoparticles, yet direct observation of the spatial relationship between the two is still lacking.[14]

In this study, the effect of nitrogen-functionalization on the nucleation and dispersion of metal nanoparticles,[25,26] and the ability of nitrogen sites to tether, *i.e.* stabilize, metal nanoparticles[26,27] are directly investigated for the first time using nanoscale electron energy loss (EEL) spectral imaging of N-implanted high-surface area carbon supports and highly oriented pyrolytic graphite (HOPG) substrates. Application of principal component analysis (PCA) and reconstruction of the spectral images derived from EELS[28–31] allowed for quantification of the nitrogen on the nanometer length-scale and establishment of a strong spatial correlation between stabilized metal catalyst nanoparticles and regions of high nitrogen content before and after electrochemical cycling. These results are combined with insights from XPS and density functional theory (DFT) simulations to identify the specific types of nitrogen functionalities that may have the most beneficial effects on catalyst stability. Finally, the benefits of nitrogen functionalization are directly demonstrated by long-term

[a]*Department of Metallurgical & Materials Engineering, Colorado School of Mines, 1500 Illinois St, Golden, CO 80401, USA. E-mail: rohayre@mines.edu*

[b]*Oak Ridge National Laboratory, 1 Bethel Valley Road, Oak Ridge, TN, 37831, USA*

[c]*Department of Chemistry, Colorado School of Mines, 1500 Illinois St, Golden, CO 80401, USA*

[d]*Mechanical Engineering Department, Stanford University, 550 Escondido Rd., Stanfordx, CA 90305, USA*

[e]*National Renewable Energy Laboratory, 1617 Cole Blvd, Golden, CO 80401, USA*

durability testing of direct methanol fuel cells (DMFC) employing both N-doped in-house catalysts and state-of the art commercial catalysts post-doped with nitrogen, which substantially outperform their respective undoped references.

Experimental

High-resolution images shown in Fig. 1 and 2c were obtained on a Hitachi model HF-3300 transmission and scanning transmission electron microscope (T/STEM) operated at 300 keV (Hitachi High Technologies North America, Pleasanton, CA). Aberration-corrected FEI Titan S 60-300 was operated at 300 kV during analysis of doped HOPG samples (Fig. 3c and d) and at 60 kV during analysis of doped carbon black samples (Fig. 2a and d). Camera length for detector angles was set at 38.00. Weighted principal component analysis (PCA) of spectral imaging datasets was performed using the Multivariate Statistical Analysis (MSA) plug-in for Digital Micrograph (from HREM Research Inc). Weighting was based on Poisson statistics.[32] Images shown in Fig. 3a and b were acquired on a Philips CM200 transmission electron microscope. TEM specimen preparation consisted of peeling off a thin top layer of HOPG graphitic sheets and positioning it between the two grids of a Cu double grid (Electron Microscopy Sciences). XPS analysis was performed on a Kratos Nova X-ray photoelectron spectrometer with a monochromatic Al K source. Data analysis was performed using CasaXPS software. A linear background was applied to N1s spectra and spectra were calibrated using the graphitic carbon peak at 284.6 eV.

Deposition of 10 wt% Pt (confirmed by TGA) onto undoped and N-doped Graphitic Vulcan supports was performed using dry impregnation of platinum precursor. $H_2PtCl_6 \cdot 6H_2O$ (from Sigma-Aldrich) was dissolved in 2 mL DI water and added to the carbon support in incremental infusions of 100–200 μL; the material was dried between infusions at 60 °C. After all of the metal precursor solution was added to the carbon support, the material was dried at 100 °C in inert atmosphere (under He) and reduced in flowing hydrogen (100% H_2) for 2 h at 200 °C, with a ramp rate 3 °C per minute.

Electrochemical durability cycling was conducted in a three-electrode aqueous electrochemical cell. The surface-modified HOPG substrate comprised the working electrode, with a Ag/AgCl reference electrode and a Pt-wire counter electrode. The experiments were conducted in 1.0 M H_2SO_4 and the potential was cycled from 0 to 1.1 V *vs.* Ag/AgCl at a scan rate of 250 mV s^{-1} for 1000 cycles. The upper potential limit of 1.1 V was implemented for Accelerated Degradation Testing (ADT). This high upper potential limit ensures that metal dissolution will be accelerated and that both the number of nanoparticles and their composition will be affected. Due to low active surface areas, the model HOPG substrates were primarily used for extensive microscopy characterization. Electrochemical measurements were performed on PtRu supported on high surface area carbon powders.[24]

Details on the synthesis, detailed characterization, MEA fabrication and MEA testing of in-house high-surface area PtRu catalyst materials discussed in Fig. 5a are presented in ref. 33 and 34. For the N-doped in-house material, ion implantation and sputtering were done back-to-back in the same chamber without breaking vacuum. Fig. 5b shows results for the unmodified commercial anode catalyst (HiSPEC 10 000 PtRu/C, Johnson Matthey, Inc.) as well as its modified version that was post-doped with nitrogen at 45 mA for 60 min. MEA fabrication and testing protocols were the same as in ref. 33. The metal loading in the first set of MEA's shown in Fig. 5a was approximately 1 mg cm^{-2} and the loading of the second set shown in Fig. 5b was approximately 3 mg cm^{-2}.

Quantum mechanical simulations have been performed using a periodic boundary condition method based on a plane wave basis set implemented in VASP.[35] Electron wavefunctions were expanded in a plane-wave basis set up to a cutoff of 400 eV using projector-augmented waves[36] with the Perdew–Burke–Ernzerhof exchange–correlation functional.[37] Methfessel–Paxton first order smearing[38] was used with a width of 0.2 eV to determine partial occupancies, and it was confirmed that the entropy TDS term was 0.5 meV per atom or less. Energy was sampled on a 6 × 6 × 1 Monkhorst–Pack[39] lattice of *k*-points, and it was verified that this did not change reported energies by more than 0.2 meV per atom compared with sampling on an 8 × 8 × 1 grid. The electronic self-consistent charge density was computed to a tolerance of 10^{-4} eV. In geometry relaxations, all atoms are allowed to relax (*i.e.* no atoms are fixed). Calculations were performed assuming non-spin polarized systems.

The adsorption energy E_{ads} of a catalyst cluster on defective HOPG (HOPG*) was calculated by

$$E_{ads} = E_{Pt_xRu_y\text{–HOPG*}} - E_{HOPG*} - E_{Pt_xRu_y}$$

where $E_{Pt_xRu_y\text{–HOPG*}}$ is the calculated energy of a Pt_xRu_y (x,y = 0,2,4) cluster adsorbed on defective HOPG, E_{HOPG*} is the calculated energy of slab of HOPG with a single defect, and $E_{Pt_xRu_y}$ is the calculated energy of a Pt_xRu_y cluster in vacuum. The dissolution energy E_{diss} for Ru in a cluser was calculated by

$$E_{diss} = E_{Pt_xRu_y\text{–HOPG*}} - E_{Pt_xRu_{y-1}\text{–HOPG*}} - E_{Ru(s)}$$

where $E_{Ru(s)}$ is the energy per atom of Ru in the solid crystalline state, and a similar procedure is used to calculate the dissolution energy of Pt.

Results and discussion

Nitrogen functionalization was accomplished in this work through ion-implantation (at low ion beam energy of 100 eV), which allows for a controlled and reproducible functionalization of the surface layers of carbon materials.[40] The nitrogen content was controlled by tuning implantation parameters such as beam current and time, which together determine the total dosage delivered to the material. Model HOPG substrates were implanted at a fixed angle of 30°, while high-surface area carbon powders were implanted using a modified in-house ion-implantation/sputtering chamber with a rotational barrel-type

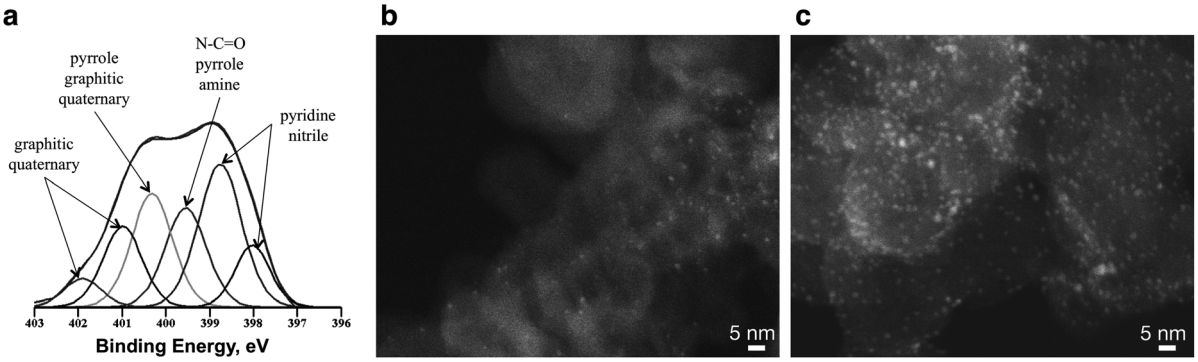

Fig. 1 (a) XPS N1s spectrum of N-doped Graphitic Vulcan. (b) HAADF-STEM image of Pt supported on undoped Graphitic Vulcan. (c) HAADF-STEM image of Pt supported on N-doped Graphitic Vulcan.

powder holder, enabling implantation to be extended to a variety of high-surface area materials, including commercially available carbon supports such as carbon blacks and even existing catalysts already loaded with metal nanoparticles to investigate effect of post-doping with nitrogen.[41]

Based on XPS analysis, ~5 at.% nitrogen is detected on HOPG after 45 s of implantation at 13 mA, while high surface area Vulcan and Graphitic Vulcan carbon blacks require significantly higher beam currents and implantation times (typically 50 mA for 1 hour) to achieve similar 5 at.% nitrogen loading. XPS analyses of all materials reveal broad N1s spectra, indicative of formation of multiple functionalities including but not limited to pyridinic, graphitic and pyrrolic groups. The N1s spectrum of 5 at.% N-doped Graphitic Vulcan (Fig. 1a) is very similar to spectra obtained and previously reported for HOPG substrates doped at saturation levels.[27,40] Previous studies have shown that low-dosage implantation primarily results in the creation of vacancies in the HOPG network along with nitrogen substitutional defects, while high-dosage increases vacancy agglomerations and pyridinic and pyrrolic nitrogen defects.[26,40,42]

It is well-known that there are significant structural differences between the major types of carbon support materials (*e.g.* graphitic *vs.* non-graphitic supports) which determine their behaviour as fuel cell catalyst supports at large.[9,43–45] The durability of carbon-supported catalysts is hampered by oxidation-induced degradation of the carbon support material itself that enhances the coalescence of catalyst nanoparticles and the densification of the electrode.[46] This degradation also causes physical detachment of nanoparticles from the support surface, with a subsequent loss of active surface area, connectivity, conductivity, as well as changes to the hydrophobic/hydrophilic balance of the surfaces.[47] The catalyst durability can be improved by employing supports with high graphitic content (such as Graphitic Vulcan), that show improved resistance against support corrosion.[43,44] However, this benefit is counterbalanced by poor metal nanoparticle wetting, nucleation and dispersion as the high graphitic content and low density of defects restricts Pt nucleation mainly to areas between carbon particles and at the edges of graphite (002) planes.[48] To investigate the effect of nitrogen doping on the nucleation of metal nanoparticles, we employed a Graphitic Vulcan doped with ~5 at.% nitrogen and used dry impregnation for metal deposition as it is suitable to demonstrate differences in nucleation site density. In order to avoid complications from the competitive nucleation and growth of Pt *vs.* Ru, in this nucleation study we focus on Pt only rather than the PtRu-alloy catalyst that is used in the durability studies discussed later in the paper. Fig. 1b demonstrates the relatively poor nucleation of Pt nanoparticles on undoped Graphitic Vulcan, where scattered nanoparticles in the size range of 1–2 nm occur primarily in association with the edges of graphitic planes. However, when the Graphitic Vulcan support material is implanted with nitrogen prior to catalyst deposition (Fig. 1c), the nucleation of uniformly dispersed Pt nanoparticles is greatly enhanced.

To further investigate the effect of nitrogen doping on Pt nucleation, and to examine the nanoscale spatial relationship between nitrogen and platinum, two types of high-resolution imaging were employed. First, the imaging of Pt atoms supported on N-doped carbon was conducted in high angle annular dark-field (HAADF) mode, which is based on incoherent scattering of electrons and derives its contrast from the differences in atomic number approximately as Z^2 on an aberration-corrected STEM platform. Second, high-resolution imaging of light elements (including carbon, nitrogen and oxygen) was performed by acquiring electron energy loss (EEL) spectral images. STEM X-ray and EEL spectral imaging produce large multidimensional datasets, and while these additional dimensions provide significant informational content, they also require efficient processing. Analysis of EEL spectral imaging data can be greatly accelerated and improved with the use of PCA; indeed it has recently been employed to reduce noise level and improve the accuracy of the background fit of EELs spectra.[30] However, because PCA has only been applied to a limited number of EELs datasets and materials systems,[28,31,49] the full capabilities of this approach are still largely unexplored and there are rich opportunities for fundamental advances that could greatly benefit materials metrology.[50] The noise level and subtle variations in EELS

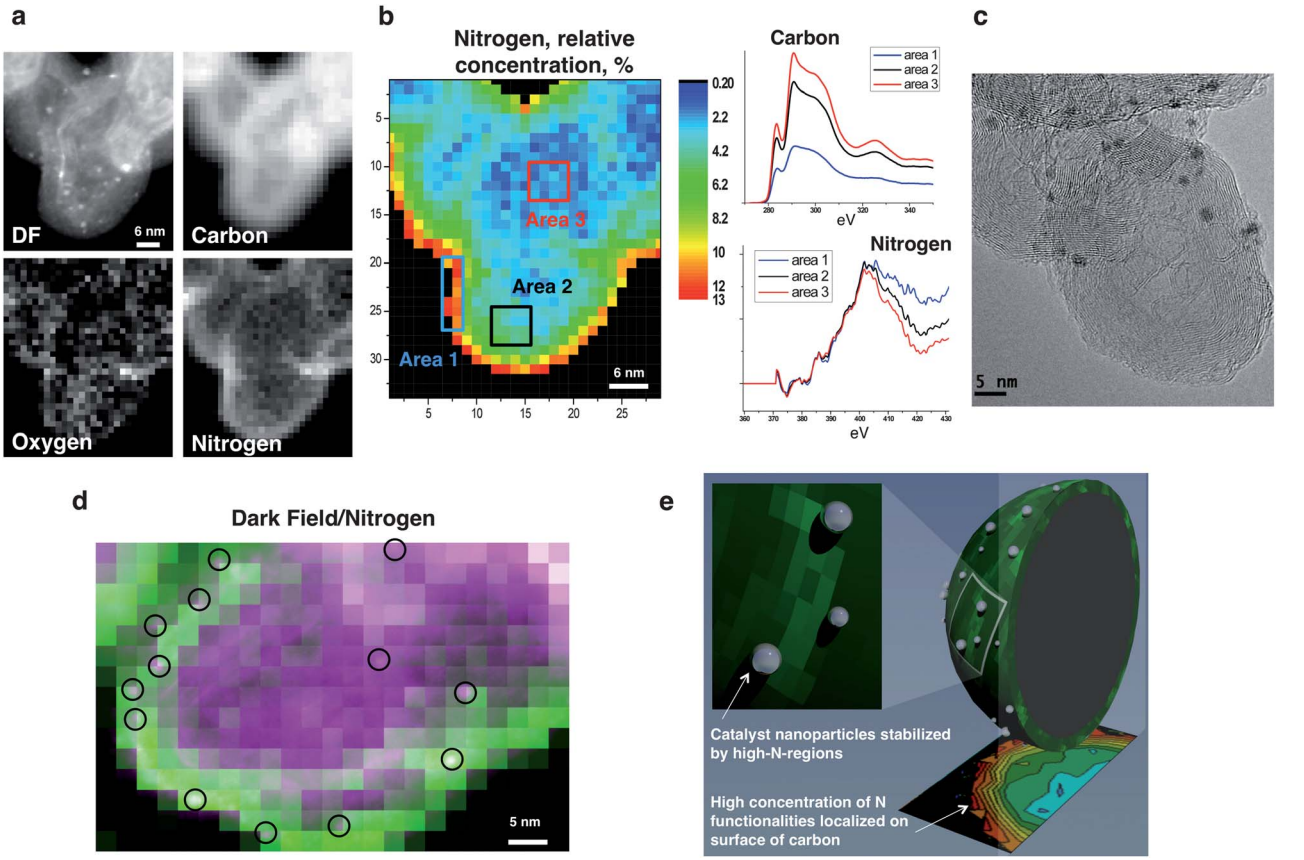

Fig. 2 (a) HAADF-STEM image and corresponding EELS oxygen, carbon, and nitrogen maps showing enrichment of the support surfaces with doped nitrogen. (b) Nitrogen map showing relative concentration of nitrogen in different regions of graphitized carbon black particle, and C K-edge and N K-edge data from three areas highlighted on the map. (c) Typical HR-TEM image of Pt/Graphitic Vulcan. (d) Overlay of HAADF-STEM (purple) and nitrogen EELS map (green) showing that metal nanoparticles primarily nucleate in regions with moderate nitrogen content, which are adjacent to the locations with the highest level of nitrogen. (e) Schematic illustration of the catalyst nanoparticle–nitrogen defect interaction model developed from these investigations.

edge intensities acquired from the N-doped samples impede facile elemental quantification and therefore, quantification of spectral images was carried out after PCA[51] analysis and subsequent reconstruction of the data.[28,31,49] Carbon, oxygen and nitrogen integrated signal maps reveal that implantation only modifies the top layers (~1 to 2 nm) of the Graphitic Vulcan carbon particles and enriches them with nitrogen (Fig. 2a and b). At regions more distant from the surface, the lower observed concentration of nitrogen is directly related to higher contributions of carbon from the bulk unmodified graphitic layers (as supported by the least change in shape of the C K-edge, Fig. 2b). The greatest modification of the graphitic carbon structure is observed at the edges (as shown by the C K-edge in Fig. 2b (area 1) and the high resolution (HR)-TEM image in Fig. 2c), where the signal is from only the outer-most layers of the graphitic planes of the support. The overlay of the HAADF and nitrogen map (Fig. 2d) demonstrates that metal nanoparticles have primarily nucleated in regions with moderate nitrogen content, adjacent to the locations with the highest level of nitrogen. This observation correlates with prior DFT simulations suggesting that on the atomic level Pt prefers to anchor to carbons neighboring the nitrogen defect sites rather than directly on the nitrogen defects themselves.[42] A schematic illustration of the catalyst-nanoparticle–nitrogen defect interaction model developed from these investigations is provided in Fig. 2e.

To facilitate direct EELS characterization with sub-nm resolution, the effect of implanted nitrogen on the stability of metal nanoparticles during electrochemical cycling was studied using well-defined planar HOPG substrates implanted with nitrogen at concentrations close to saturation levels (~7 at.%, from XPS) using conditions optimized in previous work and presented along with extensive discussion of nitrogen functionalities.[27,40] In order to compare the effect of nitrogen doping on metal nanoparticles stability separately from the effect of nitrogen doping on metal nanoparticles nucleation, sputtering rather than dry impregnation was used to introduce the metal nanoparticles onto the nitrogen-doped carbon support. Because the dry impregnation metal deposition method is sensitive to nucleation, the initial catalyst particle density, dispersion, size and composition of the catalyst nanoparticles would be drastically different on undoped and doped supports, making it difficult to de-convolve the effects of initial distribution *vs.* dopant tethering on durability. To address this issue, we

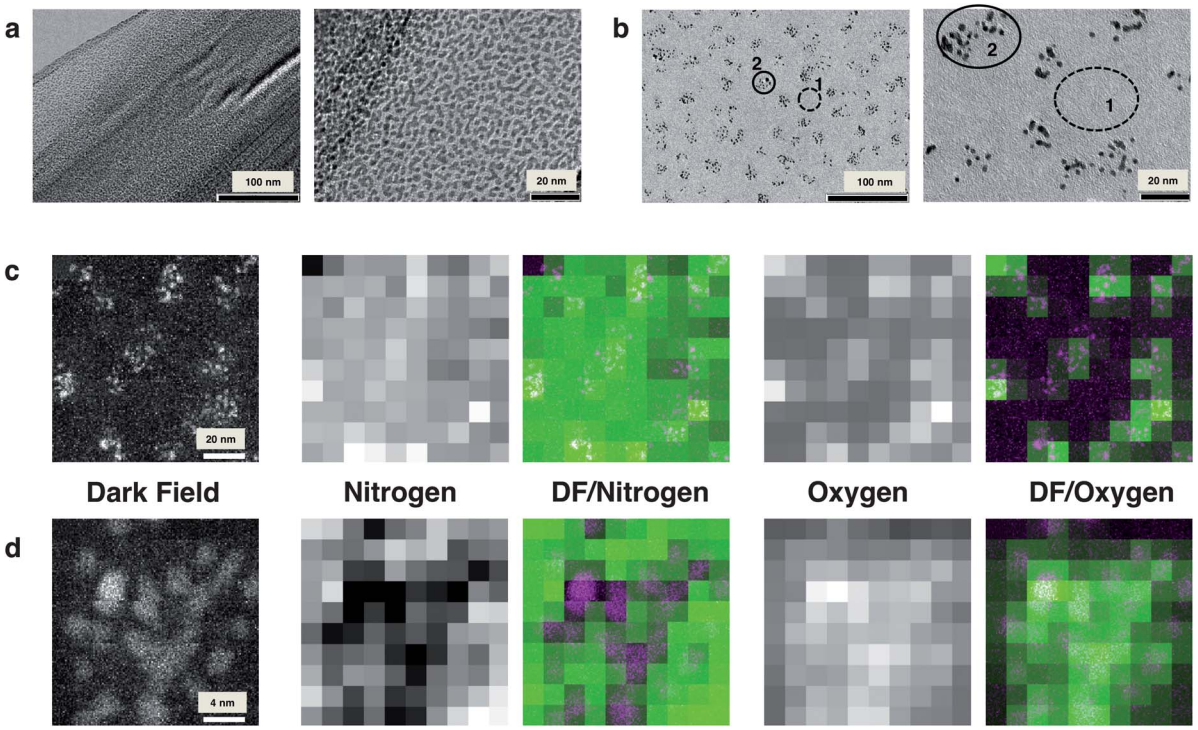

Fig. 3 Analysis of PtRu deposited on N-doped HOPG. (a) TEM images of the pre-cycled material showing initial high coverage, homogeneous spatial distribution of nanoparticles with typical size ~2 nm. (b) TEM images after post-durability potential cycling demonstrating change in nanoparticle coverage and distribution, change in the nanoparticle size, and clustering of small nanoparticles. (c and d) Show the HAADF-STEM image, nitrogen map, overlay of HAADF-STEM image (purple) and nitrogen map (green), oxygen map and overlay of HAADF-STEM image (purple) and oxygen map (green), where (c) demonstrates the spatial relationship of nitrogen/oxygen with several clusters and (d) demonstrates the spatial relationship within a single cluster.

deposited the metal nanoparticles onto the supports by sputtering from a single-alloyed alloyed PtRu target for this durability study.[27,34] We have previously demonstrated that this method enables homogeneous deposition of PtRu nanoparticles on HOPG while maintaining comparable coverage, particle density, particle size and composition irrespective of the support composition.[27]

Sputtering from a single-alloyed PtRu target onto the N-implanted HOPG substrate resulted in the formation of dispersed PtRu nanoparticles with high coverage but with little to no preferential nucleation on the N-sites (Fig. 3a). However, after electrochemical potential cycling to accelerate catalyst degradation, the catalyst distribution clearly separates into two distinctive regions, which are indicative of the heterogeneity of the catalyst–support interactions on the N-implanted HOPG substrate (Fig. 3b). In contrast, on undoped HOPG, the same electrochemical potential cycling experiment results in almost complete removal of all Pt nanoparticles (not shown). In select regions of the cycled N-doped support (such as area 1, dotted line), poor catalyst–support interaction resulted in complete detachment/dissolution of metal nanoparticles, similar to what occurs on undoped HOPG. However other regions (such as area 2, solid line) show much stronger catalyst–support interactions since the particles neither detached nor grew in size. We looked at the spatial relationship between post-cycled metal nanoparticles and nitrogen by analyzing a region containing several clusters of small PtRu nanoparticles. The nitrogen map and an overlay of the HAADF-STEM image with the nitrogen map reveal that only regions with the highest concentration of nitrogen defects offer improved catalyst–support interactions. Using a smaller probe to map nitrogen within a single cluster of small PtRu nanoparticles allows for an even more significant observation, *i.e.* PtRu nanoparticles are surrounded by (but not necessarily directly on top of) areas of the HOPG surface exhibiting higher nitrogen concentrations. Again, this finding is consistent with previous results from DFT calculations.[42] Furthermore, the spacing between the individual nanoparticles within each cluster is very similar to the inter-particle spacing observed by Zhao *et al.* for the ordering of nitrogen defects themselves in graphitic structures.[52] It is possible that at lower nitrogen doping levels, nitrogen incorporates on the same sub-lattice, and at higher dosages the nitrogen incorporates as clustered defects in a larger-scale array. In contrast, the oxygen map directly correlates with the nanoparticles due to metal oxide phases in the PtRu nanoparticles.

In order to isolate which specific nitrogen functionalities are most likely responsible for the strong nucleation and tethering effects that we have observed, DFT simulations were employed to calculate the effect of selected vacancy and nitrogen defects on the energy of adsorption and the energy of dissociation for model systems representing either Pt or PtRu on the (002)

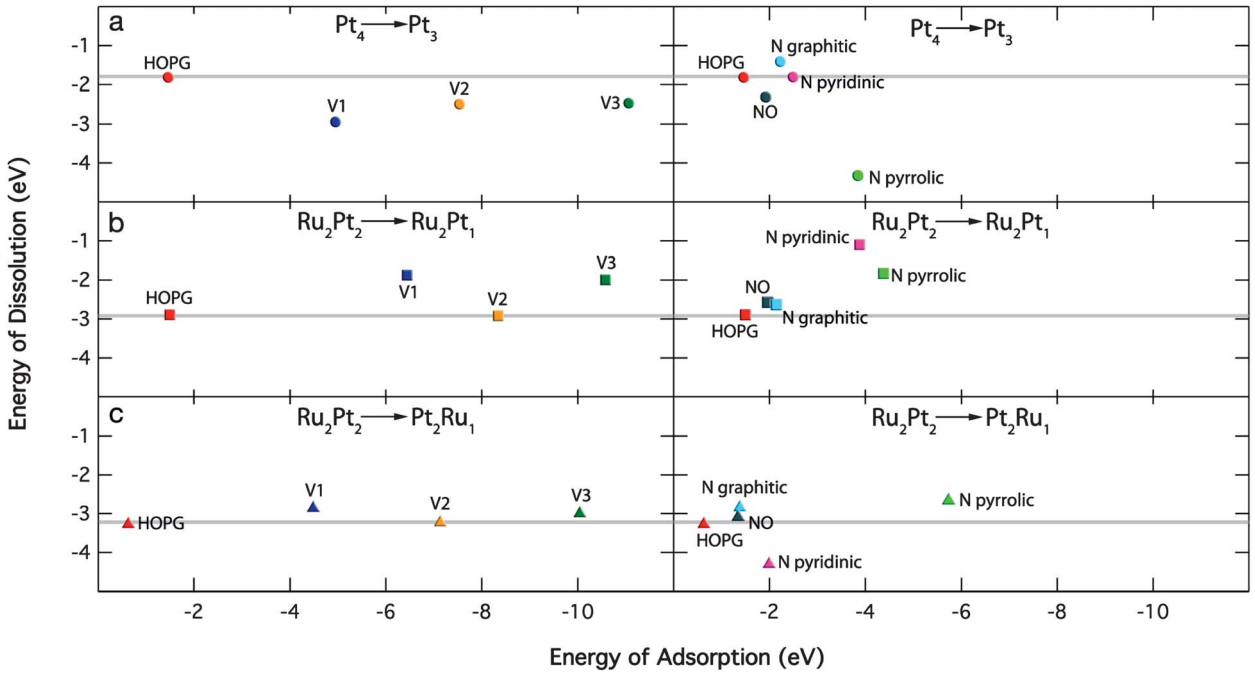

Fig. 4 Plots of binding strength *vs.* dissolution energy for HOPG, vacancies and N-defects for Pt and PtRu on different HOPG substrates. (a) Pt in Pt. (b) Pt in PtRu. (c) Ru in PtRu.

highly oriented pyrolytic graphite (HOPG) surface. Simulated defects included pyridinic ($N_{pyridinic}$), pyrrolic ($N_{pyrrolic}$), graphitic ($N_{graphitic}$) and N–O (NO) nitrogen defects, carbon vacancies (V) and clusters of two (2V) and three (3V) vacancies.[42] The results of these DFT calculations show that the energy of adsorption of metal clusters on HOPG is strongly influenced by both nitrogen defects and carbon vacancies (Fig. 1), and that clusters of vacancies appear to have the highest impact. In contrast, the energy of desorption is only slightly influenced by vacancies (V, 2V, and 3V), but nitrogen defects result in significantly larger changes in the dissolution behavior. Furthermore, this behavior is greatly affected by the specific functionality of nitrogen employed. Graphitic N defects consistently improve resistance to dissolution for all considered cases, including dissolution of Pt from Pt (Fig. 4a), dissolution of Pt from Ru_2Pt_2 (Fig. 4b) and dissolution of Ru from Pt_2Ru_2 (Fig. 4c). In contrast, pyridinic and pyrrolic nitrogen defects affect dissolution of Pt and Ru differently, indicating the importance of a selective design approach to the fabrication of nitrogen containing materials. For example, Pt catalysts should benefit most strongly from the addition of graphitic and pyridinic types of nitrogen. The stability of PtRu catalysts could most likely be improved by the addition of graphitic N and a well balanced mix of pyrrolic and pyridinic N, where pyridinic N improves stability of Pt in Ru_2Pt_2 and pyrrolic N improves stability of both Pt in Ru_2Pt_2 and Ru in Pt_2Ru_2. Nitrogen-implanted carbon supports explored in this work contain a mixture of these functionalities (Fig. 1a and ref. 27 and 40), and experimental demonstration of improved durability of PtRu nanoparticles immobilized on these supports is a great reinforcement of DFT conclusions.

In order to fully confirm the durability benefits of the nitrogen implantation treatment, two sets of prototype direct methanol fuel cells employing PtRu catalysts supported on undoped and N-doped carbon supports were subjected to durability testing at a constant cell voltage of 0.4 V for >400 h.[33] Current densities measured at 0.4 V before and after durability are compared in Fig. 5a and b. Fig. 5a compares changes in the performance of two fuel cells manufactured from in-house sputtered 30 wt% PtRu/carbon catalysts supported on undoped *vs.* N-doped Vulcan, where the nitrogen-doping was done before PtRu deposition.[33] Clearly, even after 645 h of durability testing, the fuel cell fabricated from the N-doped PtRu/C shows considerably higher performance than the undoped PtRu/C. Fig. 5b compares the performance of a fuel cell made from a state-of-the-art commercial 60 wt% PtRu/carbon catalyst that was post-modified with nitrogen to a fuel cell made from the same commercial catalyst without nitrogen modification. The overall performances of both fuel cells made from the commercial catalyst are much higher than for the in-house catalyst, in part due to higher metal loading in the catalyst materials and their respective MEA's, *yet nitrogen doping provides an even more marked benefit in this case*. In fact, the performance of the fuel cell with the N-doped commercial catalyst actually improves slightly after 425 h of durability testing, while a significant drop is observed for its unmodified counterpart. Relatively rapid decreases in performance are typically observed in long-term DMFC durability tests, so the performance stabilization achieved in the nitrogen-modified commercial catalyst is unprecedented and underscores the significant promise of this approach to improve catalyst performance and durability.

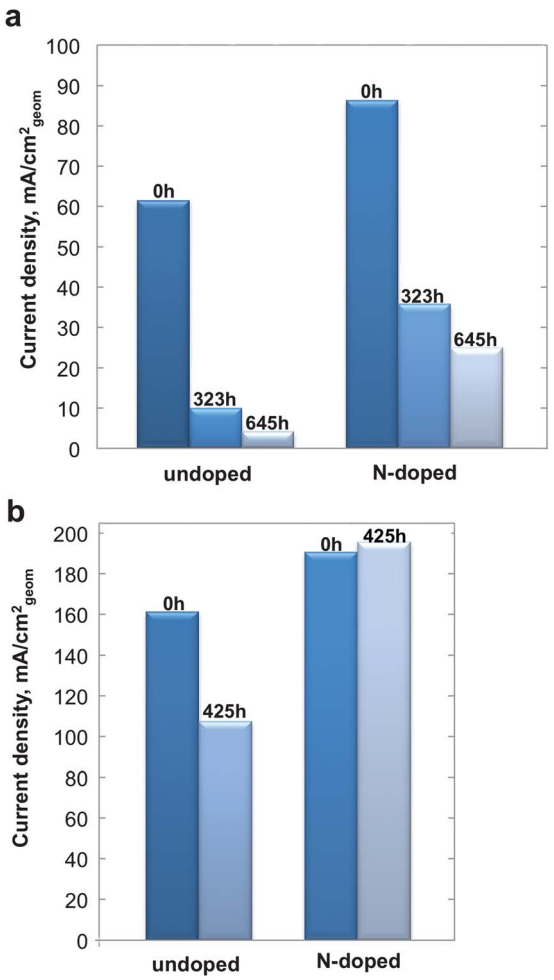

Fig. 5 MEA performance before and after durability testing for (a) in-house sputtered 30 wt% PtRu catalysts supported on undoped and N-doped Vulcan. (b) Commercial 60 wt% PtRu/carbon catalyst before and after modification with nitrogen.

Conclusions

This work has demonstrated, for the first time, a strong spatial correlation between stabilized metal catalyst nanoparticles and regions of high nitrogen content before and after electrochemical cycling and the first direct evidence of improved catalyst–support interactions related to substrate surface nitrogen content. Beneficial effects of nitrogen are supported by DFT calculations that identify the potential effects of specific types of nitrogen functionalities on catalyst–support interactions. We have applied these insights in order to functionalize state-of-the-art commercial catalysts with nitrogen and attain significant improvements in performance and long-term durability as a result. In the future, the methodology described in this work can be applied to investigate the doping of various forms of carbon including but not limited to graphene sheets, highly oriented pyrolytic graphite, carbon nanotubes, carbon aerogels and carbon blacks. Such studies will further clarify and elucidate the specific impact of nitrogen and other dopants on the properties/activity/stability/durability of various catalytic and electronic materials and may result in a next generation of "dopant-engineered" catalyst materials with even higher durability and performance metrics.

Acknowledgements

This work was supported by the Army Research Office under grant #W911NF-09-1-0528 and the U.S. Department of Energy under Contract no. DE-AC36-08-GO28308 with the National Renewable Energy Laboratory. Microscopy supported by Oak Ridge National Laboratory's Shared Research Equipment (ShaRE) user facility, sponsored by the Office of Basic Energy Sciences, U.S. Department of Energy. We acknowledge other members of the team for their contributions to this work: Katherine E. Hurst, Steven T. Christensen, Kevin O'Neill, David S. Ginley and Bryan Pivovar (NREL) and Kevin N. Wood, Prabhuram Joghee, Michael Sanders, Ryan M. Richards and Brian Gorman (CSM). We also acknowledge the surface analysis facilities at the National Renewable Energy Laboratory and the microscopy facilities at Colorado school of Mines. Computing resources were provided by the Colorado School of Mines through the Golden Energy Computing Organization (NSF grant no. CNS-0722415) and the Renewable Energy MRSEC program (NSF grant no. DMR-0820518).

Notes and references

1 S. Koh and P. Strasser, *J. Am. Chem. Soc.*, 2007, **129**, 12624–12625.
2 M. K. Debe, A. K. Schmoeckel, G. D. Vernstrorn and R. Atanasoski, *J. Power Sources*, 2006, **161**, 1002–1011.
3 M. Lefevre, E. Proietti, F. Jaouen and J. P. Dodelet, *Science*, 2009, **324**, 71–74.
4 G. Wu, K. L. More, C. M. Johnston and P. Zelenay, *Science*, 2011, **332**, 443–447.
5 F. Tao, S. Dag, L.-W. Wang, Z. Liu, D. R. Butcher, H. Bluhm, M. Salmeron and G. A. Somorjai, *Science*, 2010, **327**, 850–853.
6 J. Zhang, K. Sasaki, E. Sutter and R. R. Adzic, *Science*, 2007, **315**, 220–222.
7 V. R. Stamenkovic, B. Fowler, B. S. Mun, G. Wang, P. N. Ross, C. A. Lucas and N. M. Markovic, *Science*, 2007, **315**, 493–497.
8 F. Zaera, *Catal. Lett.*, 2012, **142**, 501–516.
9 R. Borup, J. Meyers, B. Pivovar, Y. S. Kim, R. Mukundan, N. Garland, D. Myers, M. Wilson, F. Garzon, D. Wood, P. Zelenay, K. More, K. Stroh, T. Zawodzinski, J. Boncella, J. E. McGrath, M. Inaba, K. Miyatake, M. Hori, K. Ota, Z. Ogumi, S. Miyata, A. Nishikata, Z. Siroma, Y. Uchimoto, K. Yasuda, K. I. Kimijima and N. Iwashita, *Chem. Rev.*, 2007, **107**, 3904–3951.
10 J. M. Qiu and J. P. Wang, *Adv. Mater.*, 2007, **19**, 1703–1706.
11 K. C. Neyerlin, R. Srivastava, C. F. Yu and P. Strasser, *J. Power Sources*, 2009, **186**, 261–267.
12 R. Bashyam and P. Zelenay, *Nature*, 2006, **443**, 63–66.
13 Y. Y. Shao, J. H. Sui, G. P. Yin and Y. Z. Gao, *Appl. Catal., B*, 2008, **79**, 89–99.
14 Y. K. Zhou, K. Neyerlin, T. S. Olson, S. Pylypenko, J. Bult, H. N. Dinh, T. Gennett, Z. P. Shao and R. O'Hayre, *Energy Environ. Sci.*, 2010, **3**, 1437–1446.

15 S. Maldonado, S. Morin and K. J. Stevenson, *Carbon*, 2006, **44**, 1429–1437.
16 Z. B. Lei, L. Z. An, L. Q. Dang, M. Y. Zhao, J. Y. Shi, S. Y. Bai and Y. D. Cao, *Microporous Mesoporous Mater.*, 2009, **119**, 30–38.
17 Z. B. Lei, M. Y. Zhao, L. Q. Dang, L. Z. An, M. Lu, A. Y. Lo, N. Y. Yu and S. B. Liu, *J. Mater. Chem.*, 2009, **19**, 5985–5995.
18 S. C. Roy, P. A. Christensen, A. Hamnett, K. M. Thomas and V. Trapp, *J. Electrochem. Soc.*, 1996, **143**, 3073–3079.
19 A. K. Shukla, M. K. Ravikumar, A. Roy, S. R. Barman, D. D. Sarma, A. S. Arico, V. Antonucci, L. Pino and N. Giordano, *J. Electrochem. Soc.*, 1994, **141**, 1517–1522.
20 T. Maiyalagan, *Appl. Catal., B*, 2008, **80**, 286–295.
21 G. Wu, D. Y. Li, C. S. Dai, D. L. Wang and N. Li, *Langmuir*, 2008, **24**, 3566–3575.
22 L. T. Qu, Y. Liu, J. B. Baek and L. M. Dai, *ACS Nano*, 2010, **4**, 1321–1326.
23 K. Gong, F. Du, Z. Xia, M. Durstock and L. Dai, *Science*, 2009, **323**, 760–764.
24 T. S. Olson, A. A. Dameron, K. Wood, S. Pylpenko, K. E. Hurst, S. Christensen, J. B. Bult, D. S. Ginley, R. O'Hayre, H. Dinh and T. Gennett, *J. Electrochem. Soc.*, 2013, **160**, F389–F394.
25 S. Pylypenko, A. Queen, K. C. Neyerlin, T. Olson, A. Dameron, K. O'Neill, D. Ginley, B. Gorman, S. Kocha, H. N. Dinh, T. Gennett and R. O'Hayre, *ECS Trans.*, 2010, **33**, 351–357.
26 Y. K. Zhou, R. Pasquarelli, T. Holme, J. Berry, D. Ginley and R. O'Hayre, *J. Mater. Chem.*, 2009, **19**, 7830–7838.
27 S. Pylypenko, A. Queen, T. S. Olson, A. Dameron, K. O'Neill, K. C. Neyerlin, B. Pivovar, H. N. Dinh, D. S. Ginley, T. Gennett and R. O'Hayre, *J. Phys. Chem. C*, 2011, **115**, 13676–13684.
28 U. Bangert, A. Bleloch, M. H. Gass, A. Seepujak and J. van den Berg, *Phys. Rev. B: Condens. Matter Mater. Phys.*, 2010, **81**, 245423.
29 N. Bonnet, N. Brun and C. Colliex, *Ultramicroscopy*, 1999, **77**, 97–112.
30 N. Borglund, P. G. Astrand and S. Csillag, *Microsc. Microanal.*, 2005, **11**, 88–96.
31 M. Bosman, M. Watanabe, D. T. L. Alexander and V. J. Keast, *Ultramicroscopy*, 2006, **106**, 1024–1032.
32 M. R. Keenan and P. G. Kotula, *Surf. Interface Anal.*, 2004, **36**, 203–212.
33 A. R. Corpuz, T. S. Olson, P. Joghee, S. Pylypenko, A. A. Dameron, H. N. Dinh, K. J. O'Neill, K. E. Hurst, G. Bender, T. Gennett, B. S. Pivovar, R. M. Richards and R. P. O'Hayre, *J. Power Sources*, 2012, **217**, 142–151.
34 A. A. Dameron, T. S. Olson, S. T. Christensen, J. E. Leisch, K. E. Hurst, S. Pylypenko, J. B. Bult, D. S. Ginley, R. P. O'Hayre, H. N. Dinh and T. Gennett, *ACS Catal.*, 2011, **1**, 1307–1315.
35 G. Kresse and J. Furthmuller, *Phys. Rev. B: Condens. Matter Mater. Phys.*, 1996, **54**, 11169–11186.
36 G. Kresse and D. Joubert, *Phys. Rev. B: Condens. Matter Mater. Phys.*, 1999, **59**, 1758–1775.
37 J. P. Perdew, K. Burke and M. Ernzerhof, *Phys. Rev. Lett.*, 1996, **77**, 3865–3868.
38 M. Methfessel and A. T. Paxton, *Phys. Rev. B: Condens. Matter Mater. Phys.*, 1989, **40**, 3616–3621.
39 H. J. Monkhorst and J. D. Pack, *Phys. Rev. B: Solid State*, 1976, **13**, 5188–5192.
40 S. Pylypenko, A. Queen, T. S. Olson, A. Dameron, K. O'Neill, K. C. Neyerlin, B. Pivovar, H. N. Dinh, D. S. Ginley, T. Gennett and R. O'Hayre, *J. Phys. Chem. C*, 2011, **115**, 13667–13675.
41 A. Dameron, J. Martin, S. Pylypenko, T. Olson, J. Bult, J. Leisch, K. O'Neill, R. O'Hayre, H. N. Dinh, D. Ginley and T. Gennett, *ECS Meeting Abstracts*, 2010, **1002**, 947.
42 T. Holme, Y. K. Zhou, R. Pasquarelli and R. O'Hayre, *Phys. Chem. Chem. Phys.*, 2010, **12**, 9461–9468.
43 K. Kinoshita, *Carbon: Electrochemical and Physicochemical Properties*, 1988.
44 K. Artyushkova, S. Pylypenko, M. Dowlapalli and P. Atanassov, *J. Power Sources*, 2012, **214**, 303–313.
45 K. Artyushkova, S. Pylypenko, M. Dowlapalli and P. Atanassov, *RSC Adv.*, 2012, **2**, 4304–4310.
46 P. J. Ferreira, G. J. la O', Y. Shao-Horn, D. Morgan, R. Makharia, S. Kocha and H. A. Gasteiger, *J. Electrochem. Soc.*, 2005, **152**, A2256–A2271.
47 J. Xie, D. L. Wood, K. L. More, P. Atanassov and R. L. Borup, *J. Electrochem. Soc.*, 2005, **152**, A1011–A1020.
48 K. More, *Characterization of Fuel Cell Materials, 2011 DOE Annual Merit Review, Fuels Cells and Hydrogen Technology Division*.
49 M. Bosman, V. J. Keast, M. Watanabe, D. G. McCulloch, M. Shakerzadeh, E. H. T. Teo and B. K. Tay, *Carbon*, 2009, **47**, 94–101.
50 L. Clement, C. Borowiak, R. Galand, K. Lepinay, F. Lorut, R. Pantel, G. Servanton, R. Thomas, P. Vannier and N. Bicais, *J. Phys.: Conf. Ser.*, 2011, **326**, 012008.
51 I. T. Jolliffe, *Principal component analysis*, Springer, New York, 2002.
52 L. Y. Zhao, R. He, K. T. Rim, T. Schiros, K. S. Kim, H. Zhou, C. Gutierrez, S. P. Chockalingam, C. J. Arguello, L. Palova, D. Nordlund, M. S. Hybertsen, D. R. Reichman, T. F. Heinz, P. Kim, A. Pinczuk, G. W. Flynn and A. N. Pasupathy, *Science*, 2011, **333**, 999–1003.

